Research Article | Vol. 28, No. 16 / 3 August 2020 / Optics Express 23690

Optics EXPRESS

Foveated display system based on a doublet geometric phase lens

CHANHYUNG YOO,[1,4] JIANGHAO XIONG,[2,4] SEOKIL MOON,[1,3] DONGHEON YOO,[1] CHANG-KUN LEE,[3] SHIN-TSON WU,[2] AND BYOUNGHO LEE[1,*]

[1]School of Electrical and Computer Engineering, Seoul National University, Gwanak-Gu Gwanak-ro 1, Seoul 08826, South Korea
[2]College of Optics and Photonics, University of Central Florida, Orlando, Florida 32816, USA
[3]Multimedia Processing Lab, Samsung Advanced Institute of Technology, Samsung Electronics, Suwon, Gyeonggi-do, South Korea
[4]These authors contributed equally to this work
[*]byoungho@snu.ac.kr

Abstract: We propose a new concept of a foveated display with a single display module. A multi-resolution and wide field of view (FOV) can be simultaneously achieved using only a single display, based on temporal polarization-multiplexing. The polarization-dependent lens set functions as an optical window or beam expander system depending on the polarization state, which can provide two operating modes: fovea mode for a high-resolution and peripheral mode for a wide viewing angle. By superimposing two-mode images, the proposed system supports a foveated and wide FOV image without an ultra-high-resolution display. We demonstrate the feasibility of the proposed configuration through the proof-of-concept system.

1. Introduction

The augmented reality (AR) and virtual reality (VR) market has continued to grow steadily and attracted a great deal of public interest in various fields, such as entertainment, education, medical service, and automobile industry. Recently, the rapid development of 5G wireless networks and the sudden increase of the virtual conferences due to the COVID-19 are accelerating the commercialization of AR/VR technologies [1,2]. The VR near-eye displays (NEDs) typically consist of simple optical configuration (display module and imaging lens sets), which is advantageous for providing an immersive visual experience with a wide viewing angle [3]. The released VR headsets over recent years have a field of view (FOV) of around 90~210 degrees [4–8]. The FOV of a human eye is about 150 degrees in monocular vision and 114 degrees in binocular vision [9–11], and some commercial VR products meet these FOV requirements. However, the conventional NEDs have a trade-off between FOV and angular resolution for a given display module [12]. Consequently, a wide-FOV VR device often suffers from inadequate resolution. The human visual acuity is roughly 30 cycles per degree (cpd) (i.e., 20/20 vision) [13], but most commercial products (< 10 cpd) do not support such a dense resolution [7]. In addition, the screen-door effect, which is a visual artifact that the mesh structures of the display pixel become visible, can be observed due to the low resolution [14]. The low-resolution problems may hinder visual experience in the immersed VR environment.

The resolution of the display panel must exceed 6.6K in order to simultaneously provide a wide FOV over 110° and a high resolution of 30 cpd for monocular vision, as shown in Fig. 1. The high-level resolution of a commercialized micro-display or small-sized display is around 4K [15,16], which is insufficient to meet human visual acuity. The ultrahigh density display over 8K has currently been under development, but mass production remains as a significant challenge [17–20]. The exponential increase in processing data for tremendous display pixels may hinder

#399808 https://doi.org/10.1364/OE.399808
Journal © 2020 Received 9 Jun 2020; revised 19 Jul 2020; accepted 21 Jul 2020; published 24 Jul 2020

Optics EXPRESS

a fast screen refresh and cause an operating time delay [21]. The novel driving algorithms and electronic circuit designs will be required to resolve the high demanding computation load [22–24]. In addition, other problems exist, such as low productivity, overheating of the circuit, fast data transport line, and the need to deal with a high-performance chipset for a high computational load. Even if a high-resolution display that can fulfill the human visual requirements is developed, it can still be challenging and inefficient to adopt it in VR display systems for the present.

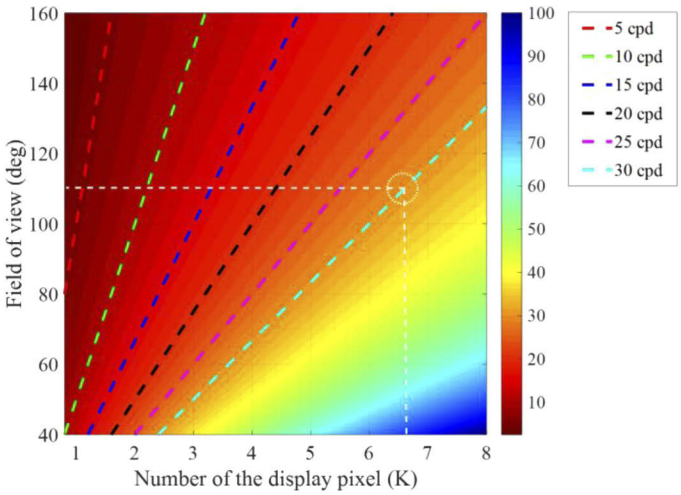

Fig. 1. Angular resolution for the VR display depending on the display resolution (x-axis) and FOV (y-axis). Each dot line indicates a boundary satisfying the specific angular resolution.

Meanwhile, the angular resolution of the human visual system depends on the viewing angle [25]. The human eye has the majority of cone photoreceptors in the center of the macula of the retina (~ 5°), which is named fovea. This region has the highest resolving power. Meanwhile, the discriminability of the eye gradually decreases outside the central vision, which is called peripheral vision [9]. Accordingly, the high-resolution images should be rendered in the fovea region. They can be replaced with low-resolution images in the peripheral area that occupies most of the visual field. This foveated imaging technique can dramatically reduce the image processing load and satisfy both a wide FOV and high-resolution conditions without ultra-high-resolution displays [26–28]. The foveated rendering solutions have already been adopted in image processing for VR applications using the eye-tracking technology [21,29]. This rendering technique maintains the resolution of the central region only to reduce the computation load of the graphics processing. In this case, the display resolution of the fovea region cannot be improved beyond the maximum resolution determined by a trade-off relationship. Several studies of foveated rendering in holographic displays have been published recently [30–32]. In addition to the software rendering technology, foveated imaging systems with multi-resolution have also been proposed [33–35]. They utilized multiple displays or optical paths for foveated imaging. These optical designs inherently have a large form factor and induce a higher material cost. AR display system with the optical zoom function using two tunable liquid crystal lenses has been proposed [36]. By adjusting the focal power of the two lenses, the size of the virtual image can be changed, which can modulate the angular resolution. However, the focal depth of the virtual image is also changed, which may not be suitable for the foveated system. In addition, the proposed liquid crystal lens has limitations in focal power, aperture size, and operation speed.

In this paper, we propose a foveated near-eye display with a single display module. Polarization-dependent lenses are adopted in our proposed system. These lenses operate in two different

Optics EXPRESS

modes by controlling the polarization state of the input beam: in the first operating mode, a high-resolution image with a narrow FOV for the fovea region, and a low-resolution image with a wide FOV for the peripheral area in the second operating mode. Both the multi-resolution and wide viewing angle are achieved with a single display by employing the time-multiplexing scheme for the two independent modes. The proposed display system is based on the retinal-projection display (i.e., Maxwellian-view display) [37–41], which can resolve the vergence-accommodation conflict (VAC) issue [42,43].

2. System configuration and display performance analysis

The proposed system is based on the polarization-dependent optical device using a geometric phase (GP) lens [44,45]. The typical liquid crystal-based GP lens has optical phase conjugation mutually as a lens depending on the polarization state of the input beam, as shown in Fig. 2(a). With left-hand circular polarization (LCP), the GP lens operates as a concave lens with a negative focal length. In contrast, the GP lens operates as a convex lens with right-handed circular polarization (RCP). The polarization-dependent lens employed in the proposed configuration has a doublet structure in which two GP lenses are sandwiched with the circular polarizer in the middle. The doublet GP lens can act in the optically transparent window mode or the lens mode depending on the polarization state of the input beam and the type of circular polarizer plate, as shown in Figs. 2(b) and 2(c). If the polarizer plate inserted between the two GP lenses is left-hand circular polarizer (LHCP), the doublet GP lens operates in the window mode for the RCP state, while it operates in the diverging lens mode for the LCP state. In contrast, if a right-hand circular polarizer (RHCP) is used, the doublet GP lens operates in the window mode for the LCP, while it operates in the converging lens mode for the RCP. This optical device can perform the multiple optical functions with a thin thickness (~ 2 mm), which has already been adopted in several studies for AR/VR displays [46–48].

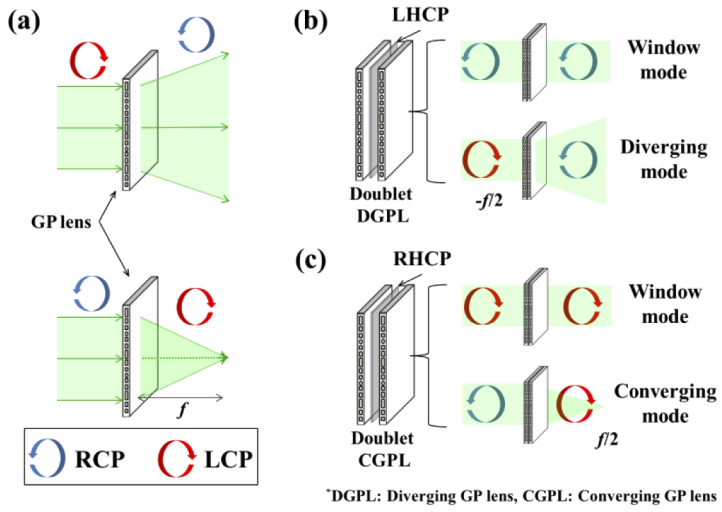

Fig. 2. Illustration of the GP lens operation depending on the polarization state of the input beam. Operating mode of (a) the single GP lens, and the doublet GP lens for (b) a diverging mode and (c) a converging mode.

Figure 3 depicts the optical configuration of the proposed foveated display for VR. The proposed system consists of a single display module, two polarization controllers, diverging and converging doublet GP lenses, and an eyepiece lens. The display module assembly for retinal-projection is based on the parallel-beam projection with a narrow beam width. In order

Optics EXPRESS

to generate collimated beam bundles, several configurations are introduced in Ref. [49]. The first polarization controller converts an input beam with random or a specific polarization state into LCP or RCP state. The second polarization controller transmits the input beam without the polarization change or changes it to the RCP state. These controllers can be implemented with a switchable active-type half-wave plate. Two polarization controllers are synchronized to combine two images in dual operating modes in real-time. The operating speed of the polarization controller determines the response time for switching between the two modes. Commercialized active polarization controllers have an operating speed of about 60 to 240 Hz, which is sufficient for providing real-time images. And finally, the eyepiece lens focuses a collimated beam, which provides a retinal-projection image by placing the eye pupil at the focal point.

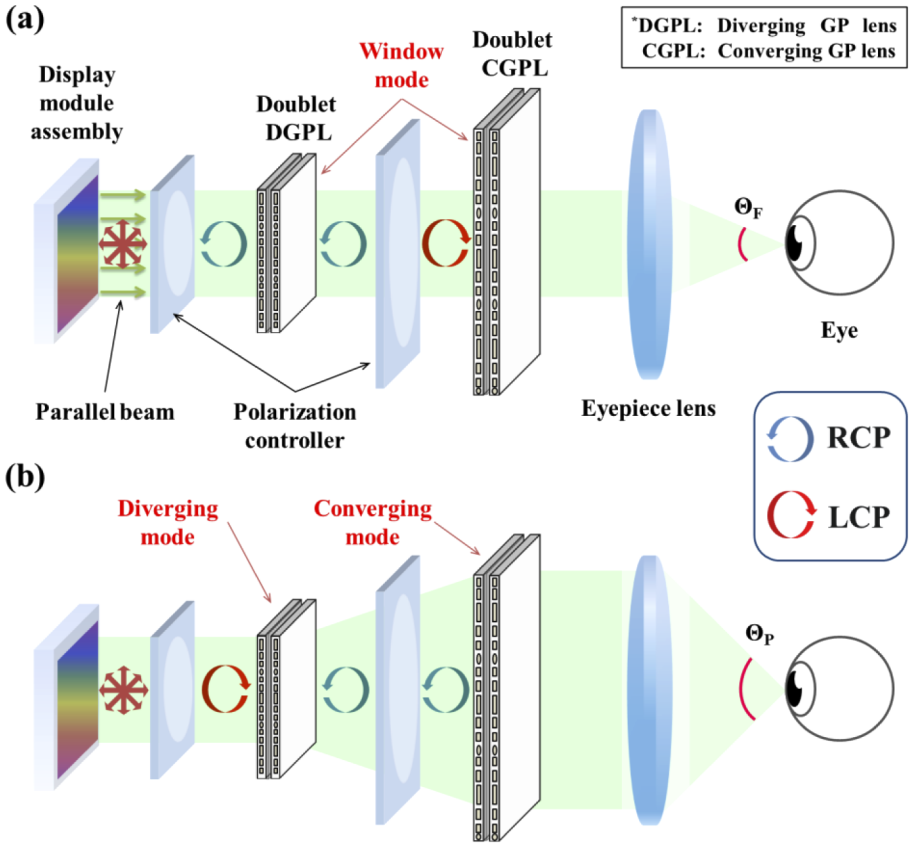

Fig. 3. Schematic diagram of the proposed foveated display for dual operating mode: (a) fovea mode and (b) peripheral mode. The polarization state is adjusted by the polarization controller for each mode. Green lines indicate the beam path through the optical elements.

The operating scheme of the system can be divided into two modes: fovea mode and peripheral mode. For a fovea mode, both doublet GP lenses operate in the window mode, as shown in Fig. 3(a). The input beam from the display module is transmitted without any optical effect, and this collimated input beam is focused by the eyepiece lens.

For a peripheral mode, two doublet GP lenses function in lens mode; the first doublet lens is a diverging lens, and the second lens is a converging lens. The polarization state of the incident beams is orthogonal to that in the fovea mode. If the focal length of the doublet GP lens for converging is identical with the negative focal distance of the diverging doublet GP lens, the divergent beam by the first doublet GP lens is converted into a magnified parallel beam

Optics EXPRESS

by the second doublet GP lens. The expanded beam for the peripheral mode enables a wider FOV compared to the fovea mode, but the angular resolution is compromised by the trade-off relationship described in Section 1. If two modes are temporally multiplexed at high speed, foveated and peripheral images can be observed simultaneously for the human eye.

In our proposed design, the ratio of the angular resolution and FOV between the two modes is determined by the focal length and aperture size of the two doublet GP lenses. Firstly, the FOV for the fovea mode (Θ_F) is simply given as:

$$\Theta_F = 2\tan^{-1}\left(\frac{S/2}{f_{ep}}\right), \tag{1}$$

where S is the size of the collimated input beam (i.e., projected image) and f_{ep} is the focal length of the eyepiece lens, which is equal to the eye relief. The magnification factor (m) for the peripheral mode can be defined as follows in the same way as the Galilean beam expander:

$$m = \left|\frac{f_{CGPL}}{f_{DGPL}}\right| = \frac{d_{CGPL}}{d_{DGPL}} \text{ for } f_{CGPL} > |f_{DGPL}|, \tag{2}$$

where f_{CGPL} and f_{DGPL} are the focal length, and d_{CGPL} and d_{DGPL} are the aperture diameter of the converging and diverging GP lens, respectively. The numerical aperture (NA) of the two doublet GP lenses should be the same to fully accept the magnified beam by the peripheral mode without loss. For the peripheral mode, the modulated FOV (Θ_P) can be calculated as follows:

$$\Theta_P = 2\tan^{-1}\left(\frac{m \cdot S/2}{f_{ep}}\right). \tag{3}$$

Secondly, the angular resolution (θ_i) for two modes can be simply expressed in cpd unit:

$$\theta_i = \frac{N_{eff}}{2\Theta_i} \text{ for } i = F \text{ or } P, \tag{4}$$

where N_{eff} is the number of the effective display pixels included in the collimated input beam. Figure 4 shows simulated results of the angular resolution depending on the magnification factor and the effective display resolution. The fixed simulation conditions are as follows: the collimating beam size S is 10 mm, and the eye relief is 20 mm. In the fovea mode (m=1), the display resolution should exceed 1685 to satisfy the angular resolution of 30 cpd or higher, and the FOV is 28 degrees. We set the angular resolution of the peripheral mode to be at least 10 cpd in consideration of the peripheral vision condition [25]. In this case, the magnification factor must be 6 or higher for a wide FOV (110°) condition in Fig. 4(b). The minimum display resolution that satisfies the three requirements concurrently is approximately 2.2K, which significantly reduces the display resolution required for the human vision compared to the conventional configuration of VR displays (~6.6K).

The optical efficiency for the proposed configuration is reduced by 50% by the circular polarizer inserted in the doublet GP lens. The optical efficiency for the overall system is reduced by 25% by two doublet GP lenses, except Fresnel loss. For an unpolarized display, the polarization controller placed between the display and the collimation lens should include a polarizer, which additionally causes 50% light loss. The overall efficiency is decreased by 12.5%. The optical efficiency issue can be resolved by replacing the circular polarizer with an active controllable retarder [50]. If the thin switchable QWP is employed, the proposed scheme can be implemented without the efficiency decrease by the circular polarizer.

Optics EXPRESS

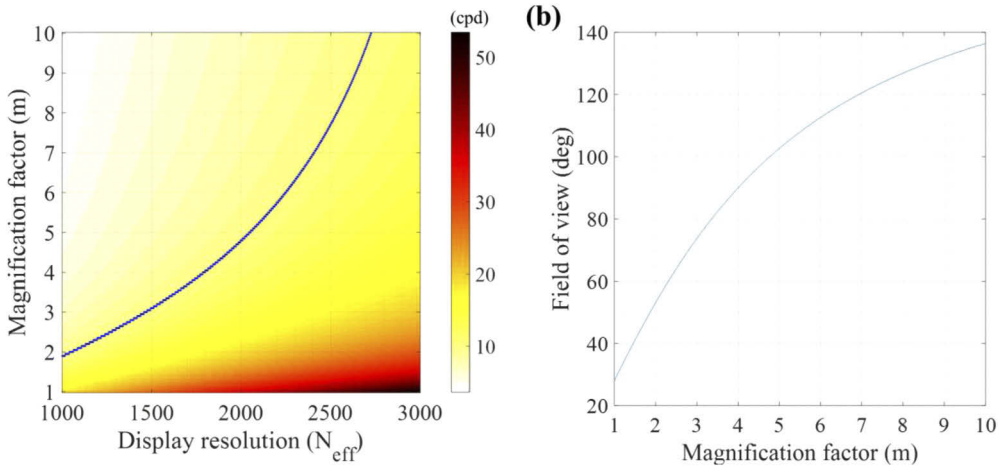

Fig. 4. Simulation results of the proposed system. (a) Contour plot of the angular resolution depending on the effective display resolution (N_{eff}) and magnification factor (m). The blue line indicates the boundary line of 10 cpd. (b) FOV results according to the magnification factor.

3. Experiment

We demonstrated our proposed configuration in experiments, as shown in Fig. 5(a). In our experiment, the laser scanning projector (Celluon PicoPro) and collimation lens are used to implement the retinal-projection display configuration with a small form factor. The laser projector has a narrow spectral bandwidth, which can alleviate the color dispersion problem. The parallel-shaped image beam is generated by placing the collimation lens at the focal length from the laser projector. The effective resolution N_{eff} is determined by the aperture size of the doublet GP lens and the specification of the display module, and can be calculated as:

$$N_{eff} = \left[2\tan^{-1}\left(\frac{d_{DGPL}}{2f_c}\right)\cdot\frac{N_{LP}}{\Theta_{LP}}\right], \tag{5}$$

where f_c is the focal length of the collimation lens, N_{LP} is the number of the original display pixels, and Θ_{LP} is the divergence angle of the laser projector. In our experiments, the display resolution of the laser projector is 1280×720, and the divergence angle is about 43°. The focal length of the collimation lens is 75 mm. The clear aperture diameter d_{DGPL} is 25.4 mm, which is the same as the effective size of the input beam (S) in Eqs. (1) and (3). According to Eq. (5), N_{eff} is 321×321 pixels based on the vertical resolution.

We fabricated two GP lenses for the converging and diverging mode, respectively, as shown in Fig. 5(b). The fabrication process began by cleaning the glass substrate with ethanol, acetone, and isopropyl alcohol. After that, a layer of photo-alignment material brilliant yellow (from Tokyo Chemical Industry, and 0.2%wt in dimethylformamide) was spin-coated onto the substrate. Next, the sample was placed under the polarization holography system for pattern exposure at 488 nm wavelength (4 mW/cm^2 for 5 min). Finally, the reactive mesogen mixture (96% of RM257, 3% of Irgacure 651 and 1% of Zonyl 8857A) was diluted in toluene with a weight ratio of 1:4 and the solvent was used for spin-coating to form the patterned liquid crystal layer. The sample was then placed under a UV lamp (365 nm) for polymerization (5 min with 10 mW/cm^2 power density). More details of the fabrication can be found in [51]. Fabricated GP lenses have a thickness between 1 and 2 mm.

Optics EXPRESS

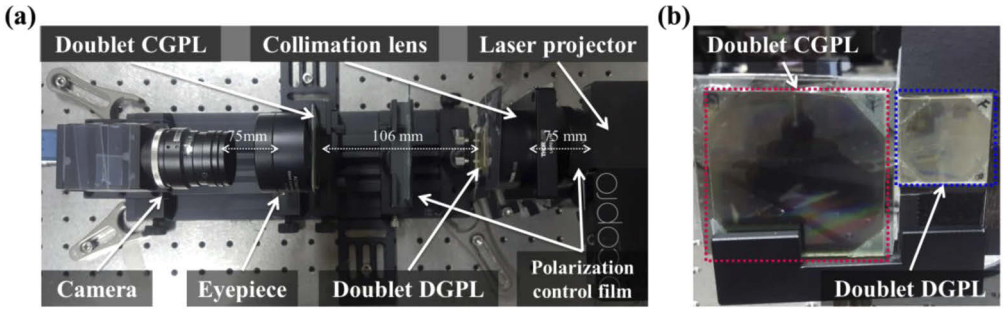

Fig. 5. (a) Experimental setup of the proposed configuration on an optical table. (b) Photograph of the fabricated doublet GP lens sets.

The focal length of the diverging doublet GP lens (f_{DGPL}) is -110 mm for 488 nm wavelengths, and that of converging doublet GP lens (f_{CGPL}) is 225 mm for 488 nm. The initially designed m factor is 2, and the f_{CGPL} should be 220 mm by Eq. (2), but there is a discrepancy of 5 mm due to the fabrication tolerance. The GP lenses for converging mode are manufactured with $d_{CGPL} = 50.8$ mm considering the m factor. The circular polarizer is employed for polarization control and manually replaced to convert each operating mode without synchronization between

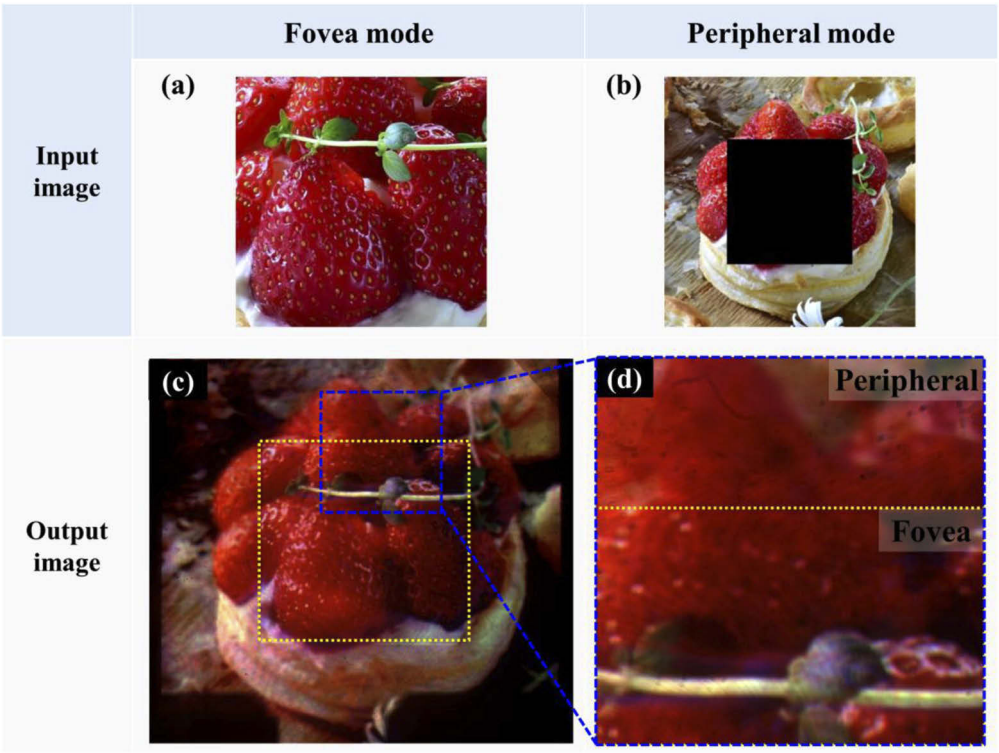

Fig. 6. Experimental results of the proposed system with ×2 magnification factor. Input display image for (a) fovea mode and (b) peripheral mode. (c) The result of the foveated image. The yellow dot lines indicate the boundary line between the two modes. (d) Magnified image (blue square) in (c).

Optics EXPRESS

the polarization controller and display module. Achromatic doublet lens with $f_{ep} = 75$ mm is employed as the eyepiece for low distortion and chromatic aberration. A CCD camera is placed after the eyepiece lens to capture the result images.

In our experimental condition, the theoretical maximum angular resolution and FOV for fovea mode is 8.3 cpd and 19.2°, and those for peripheral mode is 4.3 cpd and 37.4°, respectively. These experimental values are insufficient compared to the foveated display with wide FOV and high-resolution derived in Section 2. However, these performances can be improved by employing the following requirements: a projector display with a narrow divergence angle and GP lens sets for high m factor (~ 6).

Figure 6 shows the input images and foveated display results. Here, we use input display images with the same 321×321 resolution for two modes. As shown in Fig. 6(a), the input image for the fovea mode is cropped from the original image by m factor. In the peripheral mode, the image area corresponding to the fovea mode should be removed, as shown in Fig. 6(b). The experimental output image is obtained by digitally combining the individual result images for the fovea and peripheral modes. The foveated image region enclosed by a yellow dot line is much sharper and clearer than outside peripheral area, as indicated in Figs. 6(c) and 6(d). Therefore, this experimental result proves that the proposed foveated display has been successfully demonstrated. A discontinuity on the image is observed at a boundary line between the fovea and the peripheral region due to the drastic change of the resolution. If we further apply the Gaussian blur filter to the original image of the fovea mode, this artifact can be alleviated [35].

The modulation transfer function (MTF) is measured by calculating the contrast of the bar pattern and is presented in Fig. 7. A CCD camera lens of f /1.4 and a 25 mm focal length is used for capturing the fringe patterns. The MTF measurement is conducted under monochromatic green light. The cutoff frequency for fovea mode is about 2.7 cpd corresponding to 20% criterion, and that of peripheral mode is about 1.7 cpd.

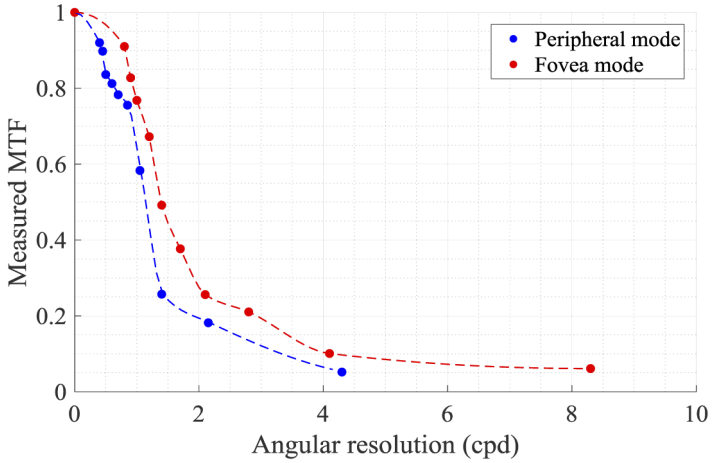

Fig. 7. MTF measurement results for the fovea and peripheral mode. The red line indicates the fovea mode, and the blue line indicates the peripheral mode.

4. Discussion of experimental results

As demonstrated above, the proposed system can support a relatively high angular resolution in the fovea region, and an expanded viewing angle with an enlarged image by a doublet GP lenses. In our experiment, the prototype system adopts a low magnification ratio (×2), but a wide FOV with a larger magnification ratio can be achieved by changing the focal length and size of the

Optics EXPRESS

GP lens. The high m factor should lengthen the distance between the two doublet GP lenses, which makes the system's form factor bulky. To reduce the system size, the GP lens should have a short focal length and a high NA. The GP lenses used in our experiment are fabricated using a photo-alignment method with liquid crystal monomers. The fabrication of a lower f-number (i.e., higher NA) lens faces the liquid crystal alignment issue when the pattern period gets smaller than the sample thickness, which can be overcome by multiple spin-coatings to reduce the sample thickness at each spin-coating. For multiple spin-coatings, f/1.0 lenses can be fabricated, which can reduce the distance between CGPL and DGPL to about 25 mm. Furthermore, GP lenses can also be fabricated through the GP-based photo-lithography, known as metalens [52]. In this case, the LC alignment issue does not exist, and the f-number can be further reduced to <0.3, which can further decrease the total system size. In addition, the optical path folding method can be employed to reduce the physical distance between the lenses [53].

In the MTF results, the resolution of the output image is deteriorated compared to the calculated MTF value by Eq. (4). The color reproduction is not also completely faithful by comparison with the original image. These degradations are caused by the following reasons. First, the fabricated GP lenses or other conventional lenses may introduce additional aberration and scattering [54]. Second, the GP lens suffers from spectral dispersion. For two wavelengths, i.e., the designed wavelength and the input beam wavelength, the focal lengths become different although the phases in GP lenses do not change much. In such a case, the focal length of the GP lens is dependent on the wavelength with the following relation [52]:

$$\frac{2\pi}{\lambda_d}\left(f_d - \sqrt{r^2 + f_d}\right) = \frac{2\pi}{\lambda_i}\left(f_i - \sqrt{r^2 + f_i}\right), \tag{6}$$

where λ_d is the design wavelength, f_d is the design focal length, r is the radial coordinate on the GP lens, λ_i is the wavelength of the input beam, f_i is the shifted focal length at each wavelength. This equation means that the focal length is approximately inversely proportional to the wavelength. When the GP lens has a doublet structure in Fig. 2, the chromatic aberration can be eliminated due to the successive conjugating operation (converging-diverging) for the see-through mode. However, the spectral dispersion is magnified twice for the lens mode. The fabricated GP lenses are designed at 488 nm, and the effective focal length of the doublet GP lens at each display wavelength is indicated in Fig. 8. The experimental setup is built on the green wavelength (527 nm), and the position of the focal spot by the chromatic aberration is shifted by -3 mm for red (640 nm) and by +2 mm for blue (445 nm) from the target 75 mm. The spot diameter fluctuates according to the wavelength at a fixed eye relief, resulting in resolution deterioration and color distortion. This chromatic aberration problem can be resolved by employing the achromatic GP lenses [55].

Third, the input beam from the laser projector has the Gaussian beam profile, and the beam diameter varies depending on the propagation distance, the focal length of the lens, and the initial beam specification for each wavelength. In the proposed configuration, the positions of the optical elements are determined by the focal length of each lens. The free variables are the distances between the collimation lens and the diverging GP lens, and between the converging GP lens and the eyepiece lens. We set both distances mentioned above to 10 mm to minimize the longitudinal size of the experimental setup. The spot size of the output beam at the retina (or camera sensor surface) w_f can be calculated as:

$$w_f = \frac{w_0' \cdot f_{eye}}{z_0'}, \tag{7}$$

where w_0' is the waist radius before passing through the eye lens (or camera lens), z_0' is the Rayleigh range before passing through the eye lens, and f_{eye} is the focal length of the eye lens. Figure 9 illustrates the calculated and measured beam spot sizes and angular resolution depending

Optics EXPRESS

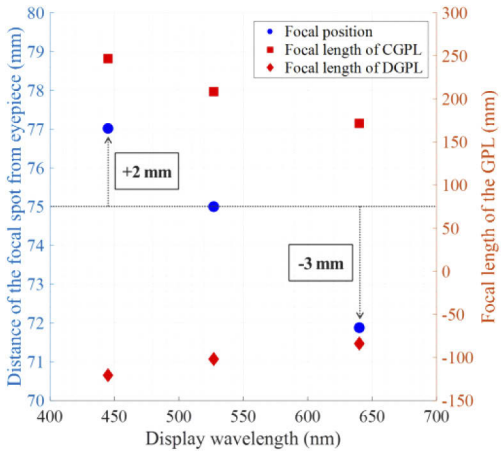

Fig. 8. Difference in focal length and position of the focal spot depending on the wavelength.

on the display wavelength and the operating mode. The measured beam spot sizes for a single pixel are acquired with a CCD camera (GS3-U3-91S6C model) with a 3.69 μm pixel pitch. The simulation results are acquired by assuming that the input beam is a Gaussian beam or ideal plane-wave-like beam. The measured beam spot in our experiment is larger than the simulation value, and the simulated beam spot for a Gaussian beam case is larger than the ideal case, as shown in Fig. 9(a). The calculated MTF for green from the single-pixel imaging-based point spread function (PSF) is indicated in Fig. 9(b) and these MTF results are similar to experimental results in Fig. 7. As a result, the Gaussian beam profile can induce degradation of the resolution compared to the ideal case. The retinal-projection display using a laser light source has an intrinsic limitation of a degraded resolution. To enhance the display resolution, the beam shaping optic, transforming the Gaussian beam to a collimated beam with uniform intensity, and other types of the display module with a non-Gaussian beam profile can be employed [56,57].

The proposed system requires an eye-gaze tracking technology to provide the high-resolution image for the fovea region according to the eye-gaze direction. In addition, the eyebox in the

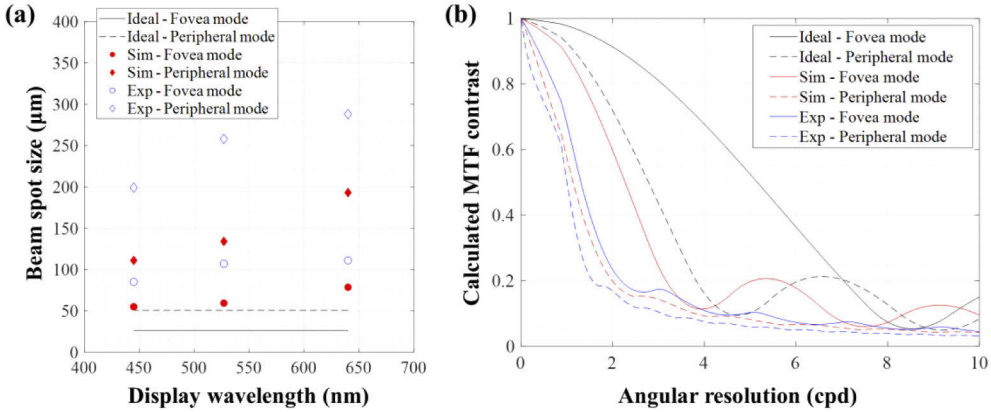

Fig. 9. (a) The diameter of the beam spot obtained by experiment and simulation. (b) Calculated MTF for green-wavelength based on the single-pixel imaging method. Ideal: simulation results for the plane-wave-like beam, Sim: simulation results for the Gaussian beam, Exp: Experimental results.

Optics EXPRESS

retinal-projection display is inherently limited to a small size near the focal spot. For expanding the eyebox, the focal spot should be shifted according to the pupil movement with pupil-tracking. A fast steering optical device or switchable image shifter can be applied to the proposed system to resolve the eyebox issue and shift for the fovea image [33,49,58,59].

5. Conclusions

In summary, we have proposed a novel foveated display with a single display module for VR applications. We used the polarization-dependent doublet GP lenses and polarization multiplexing method to implement the foveated display scheme. In a fovea mode, a high-resolution image is provided for the central region. In a peripheral mode, the virtual image is magnified by the doublet GP lenses, which provide a wide FOV image. Our proposed configuration can render a foveated image with a wide viewing angle without an ultra-high-resolution display. We have demonstrated the proposed concept in an experimental setup with passive synchronization. However, the output image obtained in our experiment has a narrow FOV and a low resolution compared to the well-designed foveated display. These experimental results can be improved by employing the GP lens set with a high NA and a high-resolution display module with a non-Gaussian beam. We expect the proposed system using the polarization multiplexing can provide an efficient alternative solution in foveated displays.

Disclosures

The authors declare no conflicts of interest.

References

1. S. Sukhmani, M. Sadeghi, M. Erol-Kantarci, and A. El Saddik, "Edge caching and computing in 5G for mobile AR/VR and tactile internet," IEEE MultiMedia **26**(1), 21–30 (2019).
2. R. P. Singh, M. Javaid, R. Kataria, M. Tyagi, A. Haleem, and R. Suman, "Significant applications of virtual reality for COVID-19 pandemic," Diabetes & Metabolic Syndrome: Clin. Res. & Rev. **14**(4), 661–664 (2020).
3. Y. Wang, W. Liu, X. Meng, H. Fu, D. Zhang, Y. Kang, R. Feng, Z. Wei, X. Zhu, and G. Jiang, "Development of an immersive virtual reality head-mounted display with high performance," Appl. Opt. **55**(25), 6969–6977 (2016).
4. P. R. Desai, P. N. Desai, K. D. Ajmera, and K. Mehta, "A review paper on oculus rift-a virtual reality headset," in arXiv:1408.1173, Aug. 2014, https://arxiv.org/abs/1408.1173.
5. P. Dempsey, "The teardown: HTC Vive VR headset," Eng. & Technol. **11**(7-8), 80–81 (2016).
6. Pimax, "Pimax 8 K Series," https://www.pimax.com/pages/pimax-8k-series.
7. Wikipedia, "Comparison of virtual reality headsets," https://www.en.wikipedia.org/wiki/Comparison_of_virtual_reality_headsets.
8. B. C. Kress, *Optical Architectures for Augmented-, Virtual-, and Mixed-Reality Headsets* (SPIE, 2020).
9. H. Stragburger, I. Rentschler, and M. Jüttner, "Peripheral vision and pattern recognition: a review," J. Vis. **11**(5), 1 (2011).
10. I. P. Howard and B. J. Rogers, *Binocular Fusion and Rivalry in Binocular Vision and Stereopsis* (Oxford University, 1995).
11. C. V. Coleman, *Visual Experiences: A Concise Guide to Digital Interface Design* (CRC Press, 2017).
12. O. Cakmakci and J. Rolland, "Head-worn displays: a review," J. Disp. Tech. **2**(3), 199–216 (2006).
13. S. H. Schwartz, *Visual Perception: A Clinical Orientation* (McGraw Hill, 2009).
14. J. Nguyen, C. Smith, Z. Magoz, and J. Sears, "Screen door effect reduction using mechanical shifting for virtual reality displays," Proc. SPIE **11310**, 113100P (2020).
15. C. Vieri, G. Lee, N. Balram, S. H. Jung, J. Y. Yang, S. Y. Yoon, and I. B. Kang, "An 18 megapixel 4.3" 1443 ppi 120 Hz OLED display for wide field of view high acuity head mounted displays," J. Soc. Inf. Disp. **26**(5), 314–324 (2018).
16. S. Kawashima, H. Shishido, S. Oshita, S. Yoshitomi, A. Yamashita, T. Ishitani, A. Sato, M. Jincho, Y. Shima, M. Katayama, and S. Yamazaki, "A 2017-ppi 4 K ultrahigh-resolution and high aperture LCD with transparent pixels using OS/OC technology," SID Symp. Dig. Tech. Pap. **48**(1), 242–245 (2017).
17. H. S. Lee, S. Jang, J. Noh, H. Jeon, B. S. Choi, Y. M. Jeon, K. Song, J. Song, H. Y. Chu, and S. Kim, "An ultrahigh density 1.96〃 UHD 2250ppi display," SID Symp," Dig. Tech. Pap. **48**(1), 403–405 (2017).
18. G. Haas, "Microdisplays for augmented and virtual reality," SID Symp," Dig. Tech. Pap. **49**(1), 506–509 (2018).
19. T. Fujii, C. Kon, Y. Motoyama, K. Shimizu, T. Shimayama, T. Yamazaki, T. Kato, S. Sakai, K. Hashikaki, K. Tanaka, and Y. Nakano, "4032 ppi high-resolution OLED microdisplay," SID Symp. Dig. Tech. Pap. **26**(3), 178–186 (2018).
20. J. Na, S. Hong, and O. Kwon, "A 2019-ppi resolution pixel circuit for high luminance uniformity of OLED microdisplays," IEEE J. Electron Devices Soc. **7**, 1026–1032 (2019).

Optics EXPRESS

21. M. Weier, T. Roth, E. Kruijff, A. Hinkenjann, A. Pérard-Gayot, P. Slusallek, and Y. Li, "Foveated real-time ray tracing for head-mounted displays," Comput. Graph. Forum **35**(7), 289–298 (2016).
22. K. Kimura, Y. Onoyama, T. Tanaka, N. Toyomura, and H. Kitagawa, "New pixel driving circuit using selfdischarging compensation method for high-resolution OLED micro displays on a silicon backplane," J. Soc. Inf. Disp. **25**(3), 167–176 (2017).
23. Y. Iwase, A. Tagawa, Y. Takeuchi, T. Watanabe, S. Horiuchi, Y. Asai, K. Yamamoto, T. Daitoh, and T. Matsuo, "A novel low-power gate driver architecture for large 8 K 120 Hz liquid crystal display employing IGZO technology," J. Soc. Inf. Disp. **26**(5), 304–313 (2018).
24. S. Park, Y. Kim, and H. Nam, "Foveation-based reduced resolution driving scheme for immersive virtual reality displays," Opt. Express **27**(21), 29594–29605 (2019).
25. P. Artal, *Handbook of Visual Optics, Two-Volume Set* (CRC Press, 2017).
26. T. Martinez, D. V. Wick, and S. R. Restaino, "Foveated, wide field-of-view imaging system using a liquid crystal spatial light modulator," Opt. Express **8**(10), 555–560 (2001).
27. R. Albert, A. Patney, D. Luebke, and J. Kim, "Latency requirements for foveated rendering in virtual reality," ACM Trans. Appl. Percept. **14**(4), 1–13 (2017).
28. B. Guenter, M. Finch, S. Drucker, D. Tan, and J. Snyder, "Foveated 3D graphics," ACM Trans. Graph. **31**(6), 1–10 (2012).
29. A. Patney, M. Salvi, J. Kim, A. Kaplanyan, C. Wyman, N. Benty, D. Luebke, and A. Lefohn, "Towards foveated rendering for gaze-tracked virtual reality," ACM Trans. Graph. **35**(6), 1–12 (2016).
30. Y. Ju and J. Park, "Foveated computer-generated hologram and its progressive update using triangular mesh scene model for near-eye displays," Opt. Express **27**(17), 23725–23738 (2019).
31. L. Wei and Y. Sakamoto, "Fast calculation method with foveated rendering for computer-generated holograms using an angle-changeable ray-tracing method," Appl. Opt. **58**(5), A258–A266 (2019).
32. C. Chang, W. Cui, and L. Gao, "Foveated holographic near-eye 3D display," Opt. Express **28**(2), 1345–1356 (2020).
33. G. Tan, Y. H. Lee, T. Zhan, J. Yang, S. Liu, D. Zhao, and S. T. Wu, "Foveated imaging for near-eye displays," Opt. Express **26**(19), 25076–25085 (2018).
34. C. Xu, D. Cheng, J. Chen, and Y. Wang, "Design of all-reflective dual-channel foveated imaging systems based on freeform optics," Appl. Opt. **55**(9), 2353–2362 (2016).
35. J. Kim, Y. Jeong, M. Stengel, K. Aksit, R. Albert, B. Boudaoud, T. Greer, W. Lopes, Z. Majercik, P. Shirley, J. Spjut, M. McGuire, and D. Luebke, "Foveated AR: dynamically-foveated augmented reality display," ACM Trans. Graph **38**(4), 1–15 (2019).
36. Y. J. Wang and Y. H. Lin, "An optical system for augmented reality with electrically tunable optical zoom function and image registration exploiting liquid crystal lenses," Opt. Express **27**(15), 21163–21172 (2019).
37. G. Westheimer, "The maxwellian view," Vision Res. **6**(11-12), 669–682 (1966).
38. Y. Takaki and N. Fujimoto, "Flexible retinal image formation by holographic Maxwellian-view display," Opt. Express **26**(18), 22985–22999 (2018).
39. J. S. Lee, Y. K. Kim, and Y. H. Won, "See-through display combined with holographic display and Maxwellian display using switchable holographic optical element based on liquid lens," Opt. Express **26**(15), 19341–19355 (2018).
40. J. Lee, Y. Kim, M. Lee, and Y. Won, "Enhanced see-through near-eye display using time-division multiplexing of a Maxwellian-view and holographic display," Opt. Express **27**(2), 689–701 (2019).
41. C. Yoo, M. Chae, S. Moon, and B. Lee, "Retinal projection type lightguide-based near-eye display with switchable viewpoints," Opt. Express **28**(3), 3116–3135 (2020).
42. G. Kramida, "Resolving the vergence-accommodation conflict in head-mounted displays," IEEE Trans. Vis. Comput. Graph. **22**(7), 1912–1931 (2016).
43. R. Konrad, N. Padmanaban, K. Molner, E. A. Cooper, and G. Wetzstein, "Accommodation-invariant computational near-eye displays," ACM Trans. Graph. **36**(4), 1–12 (2017).
44. Y. H. Lee, G. Tan, T. Zhan, Y. Weng, G. Liu, F. Gou, F. Peng, N. V. Tabiryan, S. Gauza, and S. T. Wu, "Recent progress in Pancharatnam-Berry phase optical elements and the applications for virtual/augmented realities," Opt. Data Process. Storage **3**(1), 79–88 (2017).
45. H. Yu, Z. Zhou, Y. Qi, X. Zhang, and Q.-H. Wei, "Pancharatnam–Berry optical lenses," J. Opt. Soc. Am. B **36**(5), D107–D111 (2019).
46. C. Yoo, K. Bang, C. Jang, D. Kim, C.-K. Lee, G. Sung, H.-S. Lee, and B. Lee, "Dual-focal waveguide see-through near-eye display with polarization dependent lenses," Opt. Lett. **44**(8), 1920–1923 (2019).
47. S. Moon, C.-K. Lee, S.-W. Nam, C. Jang, G.-Y. Lee, W. Seo, G. Sung, H.-S. Lee, and B. Lee, "Augmented reality near-eye display using Pancharatnam-Berry phase lenses," Sci. Rep. **9**(1), 6616 (2019).
48. W. Cui, C. Chang, and L. Gao, "Development of an ultra-compact optical combiner for augmented reality using geometric phase lenses," Opt. Lett. **45**(10), 2808–2811 (2020).
49. C. Jang, K. Bang, S. Moon, J. Kim, S. Lee, and B. Lee, "Retinal 3D: augmented reality near-eye display via pupil-tracked light field projection on retina," ACM Trans. Graph. **36**(6), 1–13 (2017).
50. H. H. Cheng, A. K. Bhowmik, and P. J. Bos, "Fast-response liquid crystal variable optical retarder and multilevel attenuator," Opt. Eng. **52**(10), 107105 (2013).

Optics EXPRESS

51. T. Zhan, J. Xiong, Y. H. Lee, R. Chen, and S. T. Wu, "Fabrication of Pancharatnam-Berry phase optical elements with highly stable polarization holography," Opt. Express **27**(3), 2632–2642 (2019).
52. G.-Y. Lee, J.-Y. Hong, S. Hwang, S. Moon, H. Kang, S. Jeon, H. Kim, J.-H. Jeong, and B. Lee, "Metasurface eyepiece for augmented reality," Nat. Commun. **9**(1), 4562 (2018).
53. E. J. Tremblay, R. A. Stack, R. L. Morrison, and J. E. Ford, "Ultrathin cameras using annular folded optics," Appl. Opt. **46**(4), 463–471 (2007).
54. J. Kim, Y. Li, M. N. Miskiewicz, C. Oh, M. W. Kudenov, and M. J. Escuti, "Fabrication of ideal geometric-phase holograms with arbitrary wavefronts," Optica **2**(11), 958–964 (2015).
55. C. Kim, S.-J. Kim, and B. Lee, "Doublet metalens design for high numerical aperture and simultaneous correction of chromatic and monochromatic aberrations," Opt. Express **28**(12), 18059–18076 (2020).
56. D. L. Shealy and J. A. Hoffnagle, "Laser beam shaping profiles and propagation," Appl. Opt. **45**(21), 5118–5131 (2006).
57. X. Ding, Y. Ren, and R. Lu, "Shaping super-Gaussian beam through digital micro-mirror device," Sci. China Phys. Mech. Astron. **58**(3), 1–6 (2015).
58. C. Knoernschild, C. Kim, F. P. Lu, and J. Kim, "Multiplexed broadband beam steering system utilizing high speed MEMS mirrors," Opt. Express **17**(9), 7233–7244 (2009).
59. N. Chen, B. Potsaid, J. T. Wen, S. Barry, and A. Cable, "Modeling and control of a fast steering mirror in imaging applications," in *Proceedings of the 6th annual IEEE Conference on Automation Science and Engineering*, Ontario, Canada, August21–24, 2010, pp. 27–32.